

# Monolithic All-Solid-State High-Voltage Li-Metal Thin-Film Rechargeable Battery

Iñaki Madinabeitia, Jokin Rikarte, Ane Etxebarria, Giorgio Baraldi, Francisco José Fernández-Carretero, Iñigo Garbayo, Rosalía Cid, Alberto García-Luis, and Miguel Ángel Muñoz-Márquez\*



Cite This: *ACS Appl. Energy Mater.* 2022, 5, 12120–12131



Read Online

ACCESS |



Metrics & More



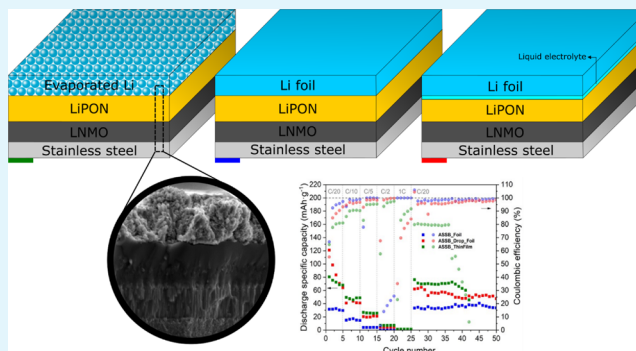
Article Recommendations



Supporting Information

**ABSTRACT:** The substitution of an organic liquid electrolyte with lithium-conducting solid materials is a promising approach to overcome the limitations associated with conventional lithium-ion batteries. These constraints include a reduced electrochemical stability window, high toxicity, flammability, and the formation of lithium dendrites. In this way, all-solid-state batteries present themselves as ideal candidates for improving energy density, environmental friendliness, and safety. In particular, all-solid-state configurations allow the introduction of compact, lightweight, high-energy-density batteries, suitable for low-power applications, known as thin-film batteries. Moreover, solid electrolytes typically offer wide electrochemical stability windows, enabling the integration of high-voltage cathodes and permitting the fabrication of higher-energy-density batteries. A high-voltage, all-solid-state lithium-ion thin-film battery composed of  $\text{LiNi}_{0.5}\text{Mn}_{1.5}\text{O}_4$  cathode, a LiPON solid electrolyte, and a lithium metal anode has been deposited layer by layer on low-cost stainless-steel current collector substrates. The structural and electrochemical properties of each electroactive component of the battery had been analyzed separately prior to the full cell implementation. In addition to a study of the internal solid–solid interface, comparing them was done with two similar cells assembled using conventional lithium foil, one with thin-film solid electrolyte and another one with thin-film solid electrolyte plus a droplet of LP30 liquid electrolyte. The thin-film all-solid state cell developed in this work delivered  $80.5 \text{ mAh g}^{-1}$  in the first cycle at  $C/20$  and after a  $C$ -rate test of 25 cycles at  $C/10$ ,  $C/5$ ,  $C/2$ , and  $1C$  and stabilized its capacity at around  $70 \text{ mAh g}^{-1}$  for another 12 cycles prior to the start of its degradation. This cell reached gravimetric and volumetric energy densities of  $333 \text{ Wh kg}^{-1}$  and  $1,212 \text{ Wh l}^{-1}$ , respectively. Overall, this cell showed a better performance than its counterparts assembled with Li foil, highlighting the importance of the battery interface control.

**KEYWORDS:** magnetron sputtering, thermal evaporation, thin-film battery, all-solid-state,  $\text{LiNi}_{0.5}\text{Mn}_{1.5}\text{O}_4$ , LiPON, stainless steel current collector



## 1. INTRODUCTION

The imminent revolution of Internet of Things (IoT), with millions of interconnected energy-demanding smart micro-devices and sensors, demands the development of a new generation of high-energy-density, long-lasting powering devices, which outperform current Li-ion batteries.<sup>1,2</sup> In this sense, the use of Li metal as an anode is living an intense upturn lately to profit from its high theoretical specific capacity ( $3,860 \text{ mAh g}^{-1}$ ), the lowest negative electrochemical potential ( $-3.040 \text{ V vs SHE}$ ), and low density ( $0.59 \text{ g cm}^{-3}$ ).<sup>3,4</sup> However, its use still entails several challenges when combined with state-of-the-art liquid electrolytes, especially related to their (i) limited electrochemical stability window, (ii) flammability, and (iii) Li dendrite formation. In this scenario, all-solid-state Li-metal batteries (ASSBs), where the liquid electrolyte is replaced by a solid Li-ion conducting material, are attracting increasing attention in order to overcome the

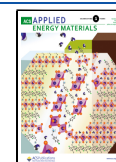
mentioned technological limits associated with liquid electrolytes. At the same time, widening the voltage stability window also opens up the possibility of working with high-voltage cathodes, paving the way for the fabrication of batteries with higher energy density, longer cycle life, and increased safety, as otherwise expected when using solid electrolytes.<sup>3,5</sup>

Two main types of materials result in mechanically and electrochemically stable Li-ion conducting solid electrolytes, namely, polymers and ceramics. On the one hand, polymer-based electrolytes have been widely reported (in particular

Received: May 23, 2022

Accepted: September 14, 2022

Published: September 27, 2022



polyethylene oxide (PEO)-based formulations) due to easy processability, low toxicity, low cost, and good chemical stability. However, they are limited by a low Li-ion conductivity at room temperature, thus forcing the cell operation at high temperatures, usually *ca.* 70 °C. On the other hand, ceramic materials are lately receiving increasing attention due to their competitive ionic conductivity, even at room temperature, as well as thermal and electrochemical stability.<sup>5</sup> Moreover, the fact that in some cases solid-state batteries have operated for more than 10,000 cycles is an irrefutable proof of the inherently slower reactivity of solid electrolytes compared to liquid ones, resulting in longer device lifetime for solid-state cells.<sup>6</sup> Furthermore, a particularly relevant advantage of ceramic electrolytes to this work is the possibility of downscaling them to thin-film format (<1 μm) for the development of all-solid-state microbatteries.<sup>7</sup> Allowing the fabrication of batteries with capacities ranging from 0.1 to 5 mAh, ideal, e.g., for IoT applications.<sup>2,8</sup>

As shown in Figure 1, all-solid-state thin-film microbatteries can be assembled as a sequential stack of thin-film layers

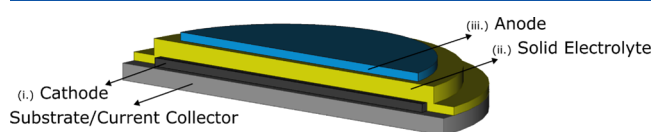


**Figure 1.** Sketch of a thin-film battery. The battery components are sequentially grown on top of a conductive substrate: (i) cathode, (ii) electrolyte, and (iii) anode. A series of shadow masks are generally employed to define the deposition areas and avoid short-circuiting both electrodes.

deposited on a substrate by means of microfabrication technologies that rely on shadow masks and selective etching processes to define the functional area of each cell component. Back in 1994, Bates and co-workers developed and patented the first thin-film microbattery, fabricated by magnetron sputtering at Oak Ridge National Laboratory (ORNL).<sup>9</sup> Notably, this coating technique is still nowadays one of the most widely used techniques for processing thin-film components owing to its high deposition rates, stoichiometry control, reproducibility, solvent-free processing, and, importantly, ability to scale-up to industrial production (e.g., roll-to-roll systems).<sup>10–12</sup> Its suitability and reliability to work with almost any type of material (conductor/insulator and crystalline/amorphous) has been demonstrated in the fabrication of different battery components: positive electrodes such as  $\text{LiMn}_2\text{O}_4$ ,<sup>13</sup>  $\text{LiCoO}_2$ ,<sup>14</sup> and  $\text{LiFePO}_4$ ;<sup>15</sup> amorphous  $\text{Li}_2\text{PO}_2\text{N}$ <sup>16</sup> and garnet-structure like  $\text{Li}_7\text{La}_3\text{Zr}_2\text{O}_{12}$ <sup>17</sup> solid electrolytes; negative electrodes such as  $\text{Li}_4\text{Ti}_5\text{O}_{12}$ <sup>18</sup> and  $\text{SnO}_2$ ,<sup>19</sup> and metallic current collectors such as Ag, Cu, or Al.<sup>20</sup>

Nowadays, the portfolio of thin-film materials is very broad. Most of the studies are focused on the advanced cathode characterization, with metallic lithium as the anode and lithium phosphorous oxynitride ( $\text{Li}_3\text{PO}_4\text{-xN}_x$ , commonly referred as LiPON) as the solid electrolyte. Despite the progress made in the development of new materials, nowadays the most used inorganic solid-state electrolyte material in thin-film form is LiPON. Using LiPON as an electrolyte allows widening the voltage stability window of the cells up to 5.5 V,<sup>21</sup> enabling the integration of high-voltage positive electrodes<sup>22</sup> and paving the way toward fabrication of high-energy-density batteries.<sup>3</sup> Its stability against metallic Li and negligible electronic con-

ductivity ( $>10^{14} \Omega \text{ cm}$ ) are key aspects here, while its main drawback is the relatively low ionic conductivity ( $2 \times 10^{-6} \text{ S cm}^{-1}$  at room temperature).<sup>23</sup> Many research efforts around this solid electrolyte have been primarily focused on increasing its ionic conductivity by varying deposition conditions, such as the sputtering power,  $\text{N}_2$  pressure, and substrate temperature.<sup>24–26</sup> However, it is to be noted that a drastic thickness reduction of the electrolyte layer eventually permits its practical use, regardless of the lower conductivity. Finally, regarding the Li metal anode, the most widely used way to deposit the lithium thin layer is by thermal evaporation, although its deposition details or characteristics are rarely given. The most commonly used positive electrodes such as olivine  $\text{LiFePO}_4$ , spinel  $\text{LiMn}_2\text{O}_4$ , or layered  $\text{LiCoO}_2$  have a limited working voltage of 3.5, 4.2, and 4.2 V vs  $\text{Li/Li}^+$ , respectively.<sup>14,15,27</sup> In this sense, the cobalt-free  $\text{LiNi}_{0.5}\text{Mn}_{1.5}\text{O}_4$  (LNMO) was proposed as a very promising alternative for the next generation of high-power thin-film, providing a high working voltage of 4.7 V vs  $\text{Li/Li}^+$  (corresponding to two redox couples of nickel) that results in a high energy density (specific capacity of  $C_{\text{theo.}} = 146.6 \text{ mAh g}^{-1}$ ), high charge/discharge rate capability, an acceptable electronic and Li-ion conductivities.<sup>28–30</sup>

In 2012, the combination of LNMO and LiPON was explored by Baggetto and co-workers at ORNL. The coating of LNMO with LiPON was found to result in the reduction of Coulombic losses and in improved rate capability when tested using  $\text{LiPF}_6$  dissolved in an organic carbonate-based liquid electrolyte and Li metal as the negative electrode.<sup>31,32</sup> The same authors also studied the influence of metal oxide coatings on LNMO thin-film electrodes when cycled using a liquid electrolyte.<sup>33</sup> Other authors have reported the electrochemical response of epitaxial LNMO (100) grown on  $\text{LaNiO}_3$  (100) current collectors that have been deposited on Nb-doped  $\text{SrTiO}_3$  (100) substrates; in this case, amorphous  $\text{Li}_3\text{PO}_4$  was used as an electrolyte and Li metal as a negative electrode.<sup>34</sup> So far, the best-performing LNMO thin-film cell with a LiPON electrolyte and a Li metal anode was grown on Pt-coated  $\text{Al}_2\text{O}_3$  substrates.<sup>6</sup> Besides LNMO,  $\text{LiCoPO}_4$  has been used as a positive electrode (4.8 V vs  $\text{Li/Li}^+$ ) in thin-film batteries with LiPON as the electrolyte and Li metal as the anode,<sup>35</sup> in this case, though, the highest conductive phase appeared only at 2.5 V.

Despite the intensive efforts devoted toward the development of solid-state batteries and the identified gaps in terms of materials science, processing science, and design engineering,<sup>36</sup> the poor interconnection of the solid–solid electrode–electrolyte interface is often cited as the main limitation for full exploitation of the electrochemical properties of electroactive materials.<sup>3</sup> The poor adherence generated by discontinuities at the interface results in limited diffusion paths of Li ions<sup>37</sup> that is often addressed by integrating liquid or gel catholytes in the system, thus deviating from the pure solid-state concept. Moreover, the appearance of detrimental reaction products at the inner battery interfaces, predominantly between the Li metal and the solid electrolyte, is usually behind the high internal resistance of the cell that ultimately reduces the cell performance.<sup>38</sup> In this regard, it is worth mentioning that low interface resistance in solid-state thin-film batteries with the LNMO electrode and  $\text{Li}_3\text{PO}_4$  electrolyte has already been demonstrated. However, the Li metal–solid electrolyte interface is still an open question.<sup>39</sup>

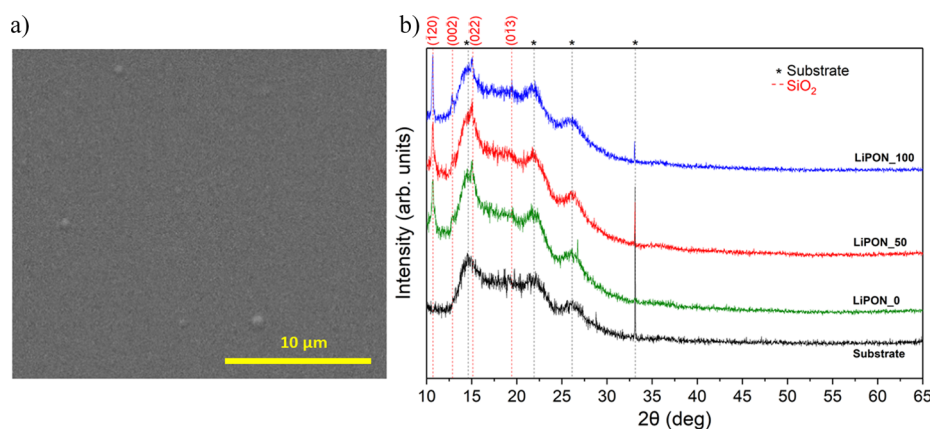


**Figure 2.** (a) Top-view SEM images of LiPON<sub>50</sub> thin film and (b) X-ray diffraction patterns for LiPON<sub>0</sub>, LiPON<sub>50</sub>, and LiPON<sub>100</sub>.

In this work, a thin-film ASSB comprising a high-voltage cathode LNMO, a LiPON ceramic electrolyte (both deposited by magnetron sputtering), and a metallic Li anode (thermally evaporated) has been developed. All was sequentially deposited on functional and cost-effective stainless-steel current collector ( $\sim 1.5 \text{ kg}^{-1}$ ), starting from the cathode. The structural and electrochemical properties of each electroactive component of the battery have been analyzed separately before the building up of the cell. The optimization of the cathode has been described in a previous work.<sup>40</sup>

## 2. EXPERIMENTAL SECTION

**2.1. Cathode Fabrication.** LNMO deposition was performed by a CemeCon MF-AC dual technology-based magnetron sputtering system on low-cost stainless-steel discs (316L, Hohsen Corp.) using a 12 mm circular mask. The selected growth parameters are detailed in a previous work focused on the optimization of LNMO thin-films.<sup>40</sup> Under these conditions, an  $8.91 \text{ nm min}^{-1}$  deposition rate and a good film adhesion were achieved. The growth process lasted for 2 h, leading to the deposition of  $1.07 \pm 0.02 \text{ } \mu\text{m}$ -thick films. After deposition, the LNMO film was annealed up to  $600 \text{ }^\circ\text{C}$  for 1 h in air to achieve a desired crystallographic structure using a heating ramp of  $5 \text{ }^\circ\text{C min}^{-1}$  and cooling down slowly inside the switched off oven.

**2.2. Solid Electrolyte Fabrication.** LiPON thin-film electrolytes were deposited by radio frequency (RF) reactive magnetron sputtering with an integrated full-face erosion technology, wherein the whole target surface is sputtered via motor-driven dynamic plasma scanning. In this way, it was possible to increase the deposition rate and homogeneity of the thin film across the deposition area. A power density of  $1.09 \text{ W cm}^{-2}$  was applied to a 3 in.  $\text{Li}_3\text{PO}_4$  circular target (Toshiba Manufacturing Co.). The substrate-to-target distance was 90 mm with an incident angle of  $45^\circ$ . During the sputtering process, a working pressure of  $4.5 \times 10^{-3}$  mbar of Ar and  $\text{N}_2$  was kept constant. In order to analyze the role of the nitrogen concentration on the solid electrolyte, different percentages of pure nitrogen ( $\text{N}_2$ ) flow rates were used: 0, 50, and 100%. These samples are henceforth referred as LiPON<sub>0</sub>, LiPON<sub>50</sub>, and LiPON<sub>100</sub>, respectively. Sixteen-hour-long processes were carried out, leading to  $1.3 \text{ } \mu\text{m}$ -thick solid electrolyte layers.

The LiPON thin films were grown on atomically flat Si (100) single-crystal substrates for morphological, structural, and elemental characterization. SEM (FEI quanta-200FEG) was used to measure the thickness and surface morphology. The crystallographic structure study has been carried out by X-ray diffraction (XRD) using a Bruker Advance D8 diffractometer with Cu radiation ( $\text{Cu K}\alpha_{1,2} \lambda = 1.5406$  and  $1.5444 \text{ \AA}$ ). The study was conducted at  $2\theta$  angles ranging from  $15$  to  $65^\circ$   $2\theta$  with a step size of  $0.02^\circ$ . The resulting diffractograms were interpreted using both the diffraction data found in the literature and the Diffract.eva software. The elemental composition of the surface of

phosphorous oxide and oxynitride samples was analyzed by X-ray photoelectron spectroscopy (XPS) using a Phoibos 150 spectrometer (Specs GmbH) in fixed analyzer transmission mode and a non-monochromatic Mg  $\text{K}\alpha$  X-ray source ( $h\nu = 1253.6 \text{ eV}$ ) operated at 100 W. Survey spectra were obtained with  $0.5 \text{ eV}$  step size and a pass energy of  $50 \text{ eV}$ . Particular regions of O 1s, N 1s, C 1s, P 2p, and Li 1s were acquired with high resolution: a step size of  $0.1 \text{ eV}$  and a pass energy of  $30 \text{ eV}$ . Experimental data was treated with CasaXPS software. The zero of binding energy for all the spectra was calibrated using the aliphatic carbon signal, which was set at  $284.6 \text{ eV}$ .

In order to evaluate the ionic conductivity of the electrolyte, LiPON thin films were deposited on  $10 \times 10 \times 0.5 \text{ mm}$  dielectric MgO (100) single-crystal substrates (CrysTec GmbH). Here,  $6 \times 1 \text{ mm}$ - and  $440 \text{ nm}$ -thick copper electrodes were deposited on top of the LiPON films by means of direct current (DC) magnetron sputtering and using a shadow mask. An air-tight Linkam HFS600E-PB4 stage was used for the in-plane ionic conductivity measurements. Impedance measurements were carried out with the help of a Biologic EC-Lab potentiostat in the frequency range from  $7 \text{ MHz}$  to  $100 \text{ mHz}$ , with 10 points per decade and a sinus amplitude of  $20 \text{ mV}$ . The conductivity measurements were performed at temperatures of  $150$ ,  $200$ , and  $250 \text{ }^\circ\text{C}$  under a controlled Ar atmosphere within the Linkam stage.

**2.3. Anode Fabrication.** The lithium metal anode was deposited by thermal evaporation using commercial crucibles from AlfaSources (AlfaVakuo e.U.) that contained the evaporation material. Prior to the lithium deposition, the evaporation chamber was evacuated down to a base pressure below  $1 \times 10^{-8}$  mbar, the substrate-to-crucible distance was set at  $50 \text{ mm}$ , and a current of  $12 \text{ A}$  was applied to the crucible that contains the lithium. During the deposition, a working pressure of  $5 \times 10^{-8}$  mbar was maintained for a 24 h-long process that resulted in a  $1 \text{ } \mu\text{m}$ -thick lithium film.

For the transport and handling of the air-sensitive samples, air-tight transfer arms and an inert atmosphere glove box (Ar filled, with  $\text{H}_2\text{O}$  and  $\text{O}_2$  concentrations below  $0.1 \text{ ppm}$ ) were used.

**2.4. All-Solid-State Thin-Film Battery Fabrication.** The assembly of the monolithic all-solid-state battery was performed following a sequential process in which the different components were grown layer by layer. First, the LNMO thin-film cathode was deposited on top of the SS substrate using the  $12 \text{ mm}$  diameter shadow mask followed by a post-annealing process in order to achieve the desired crystallographic structure. On top of that, the LiPON thin-film electrolyte was deposited; in this case, no shadow masks were used, thus a full coverage of the LNMO/SS sample was attained. Finally, the lithium anode was deposited by thermal evaporation over the electrolyte, this time using again a circular shadow mask with a  $12 \text{ mm}$  diameter hole.

By means of an air-tight transfer tool, the resulting all-solid-state cell was transferred into an Ar-filled glove box where it was sealed in a pouch cell (image of the cell included in the last section of the Supporting Information file, Figure S7a). The finalized cells were

connected to a MACCOR battery cyler, which is placed in a laboratory with controlled temperature (25 °C), to perform galvanostatic cycling. For these tests, the voltage window was in the 3.5–5 V range and the current rates were set in the C/20 to the C range. Specific capacities and currents were determined with respect to the exact mass of the positive electrode loading. The electrochemical performance data of the ASSB cell was compared with data obtained after performing the same electrochemical tests on cells assembled using conventional lithium foil as an anode and after incorporating a drop of liquid electrolyte (1 M LiPF<sub>6</sub> in dimethyl carbonate (DMC) and ethylene carbonate (EC) (1:1 v/v, Solvionic, 99.9%)) in the interface between the solid electrolyte and the lithium foil.

### 3. RESULTS AND DISCUSSION

**3.1. Solid Electrolyte Characterization.** The surface morphology of the electrolyte films has been evaluated by means of SEM. While the surface of the sample deposited only with argon is granulated, a smoother surface was obtained when increasing the nitrogen flow (Figure 2a) (images included in the Supporting Information, Figure S1). Nevertheless, from a morphological point of view, all films presented a dense and homogeneous structure required.

X-ray diffraction measurements confirmed the expected amorphous nature of the LiPON thin films prepared in this work (Figure 2b). As it can be seen in the diffraction pattern, only those peaks related to the silicon substrate and Kapton film used for sample protection (see diffraction pattern from the reference substrate in black, Figure 2b) were observed for all the samples. Meanwhile, no peaks associated with electrolyte crystallinity could be identified, confirming the amorphousness of the LiPON films. This statement is in line with the reported literature on LiPON thin-film layers deposited by RF magnetron sputtering.<sup>41,42</sup> The presence of orthorhombic SiO<sub>2</sub> (ref. COD 4110502) is worth mentioning,<sup>43</sup> with diffraction peaks located at 10.6, 12.8, 15.1, and 18.9° 2θ, which has been formed during deposition. In any case, the SiO<sub>2</sub> formation would be associated with the use of Si as the substrate and would not be present when moving to the functional SS substrate.

In order to identify any change related to the insertion of nitrogen into the structure, surface elemental characterization was performed by means of XPS. Figure 3 shows the XPS spectra of the O 1s, N 1s, P 2p, and Li 1s regions for LiPON<sub>0</sub>, LiPON<sub>50</sub>, and LiPON<sub>100</sub> films.

As expected, the major difference between N-containing and N-free electrolyte films becomes visible when analyzing the N 1s region. While the film deposited using only Ar as background gas (LiPON<sub>0</sub>) shows no N 1s peak, the other two samples are characterized by a broad N 1s photoelectron peak that can be resolved with two different components. This is in agreement with previous reports,<sup>26,44</sup> where the two N 1s components are ascribed to a doubly coordinated nitrogen –N= (labeled as N<sub>d</sub>) and a triply coordinated nitrogen –N< (labeled as N<sub>t</sub>), as otherwise expected for LiPON (see Figure S2 in the SI). Additionally, a weak peak at a higher binding energy (around 403 eV) can be seen, probably corresponding to O–N=O (N<sub>o</sub>).<sup>45</sup> In both cases, N<sub>d</sub> presents a more intense signal than the N<sub>t</sub> contribution, indicating a relatively higher concentration in the glass structure, with N<sub>d</sub>/N<sub>t</sub> being about 2.39 for LiPON<sub>50</sub> and 3.42 for LiPON<sub>100</sub>. Notably, an increase in doubly coordinated nitrogen is observed when the amount of nitrogen in the system is increased. When comparing the two nitrated samples, LiPON<sub>50</sub> and

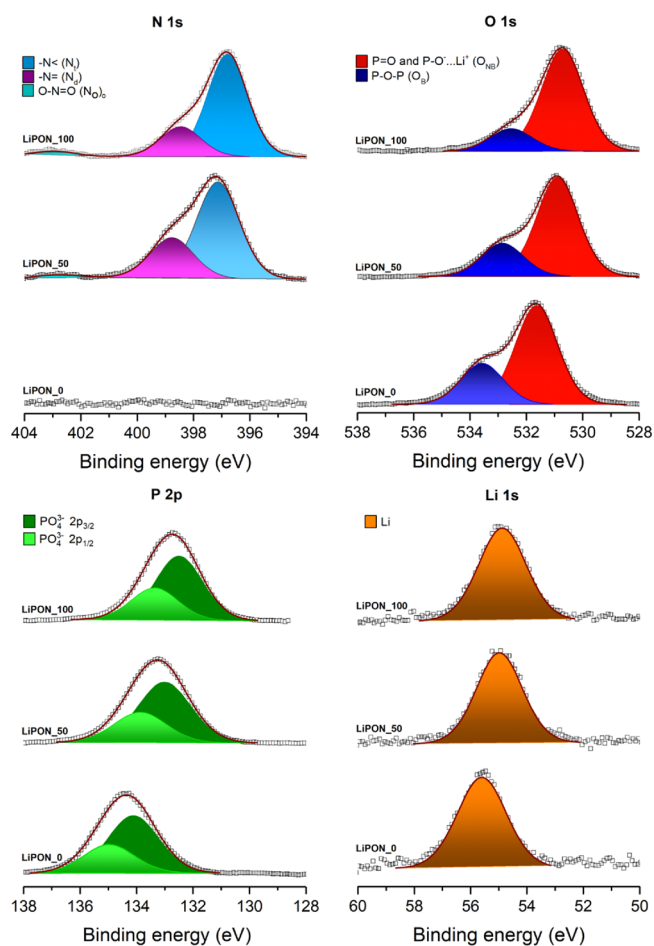


**Figure 3.** XPS profiles deconvolution of the regions O 1s, N 1s, P 2p, and Li 1s for LiPON<sub>0</sub>, LiPON<sub>50</sub>, and LiPON<sub>100</sub> samples. Note that the ordinate axes, which correspond to the normalized photoelectron intensity in arbitrary units, have not been incorporated in the graph for a better visualization.

LiPON<sub>100</sub>, a clear shift toward lower binding energies can be observed when increasing N content. This way, the doubly coordinated nitrogen shifts from 397.1 eV in the case of LiPON<sub>50</sub> and to 396.8 eV in the case of LiPON<sub>100</sub>, while the less intense triply bonded nitrogen contribution shifts from 398.8 to 398.5 eV. N<sub>o</sub> also presents a similar shift, from 403.0 eV for LiPON<sub>50</sub> to 402.90 eV for LiPON<sub>100</sub>. This slight binding energy shift can be associated with a decrease in the surface charge load associated to the electro-insulating nature of these oxides.<sup>46</sup>

The analysis of the O 1s spectrum has been carried out using the model proposed by Brow et al.,<sup>47</sup> where the main contribution at low binding energies (ca. 531 eV) corresponds to the non-bridging oxygen (O<sub>NB</sub>), whereas the shoulder located at high binding energies (around 533 eV) corresponds to a bridging oxygen (O<sub>B</sub>). As described in the literature,<sup>48,49</sup> the O<sub>NB</sub> contribution could be interpreted as the sum of two types of non-bridging oxygens present in lithium phosphate oxide and oxynitride structures, P=O and P–O<sup>−</sup>...Li<sup>+</sup>.

Like the abovementioned case, introducing nitrogen into the system entails a slight displacement toward low binding energies for both the non-bridging (531.6 > 530.9 > 530.7 eV for LiPON<sub>0</sub>, LiPON<sub>50</sub>, and LiPON<sub>100</sub>, respectively) and bridging (533.6 > 532.8 > 532.6 eV) oxygens. Similarly, as the nitrogen is inserted in the phosphate base glass, the area of O<sub>B</sub>

decreases about that of  $O_{NB}$ . In the sample LiPON\_0, the  $O_B/O_{NB}$  ratio is 0.42, close to the theoretical ratio of 0.50 for a metaphosphate glass;<sup>47</sup> while for 50% of nitrogen, the ratio is reduced to 0.33; finally, for 100% nitrogen, it reduces to 0.22. In order to provide a theoretical estimation of the efficiency of oxygen incorporation in the LiPON structure, two structural models will be used. The first one is related to the specific region of O 1s as proposed by Brow et al.<sup>47,48</sup> (eq 1)

$$\frac{O_B}{O_{NB}} = \frac{1 - 3z_i/4}{1/y_0 - 3z_i/4} \quad (1)$$

where  $y_0$  is the  $O_B/O_{NB}$  ratio for the non-nitridated sample (LiPON\_0) and  $z_i$  is the N/P ratio of the nitridated sample under consideration. In this model, it is assumed that nitrogen has no preference in replacing either bridging or non-bridging oxygens, *i.e.*, equal numbers of these species are replaced during nitridation.

The second model, proposed by Marchand et al.,<sup>49</sup> correlates the amount of doubly and triply coordinated nitrogen in the sample under consideration with the amounts of non-bridging and bridging oxygen, based on the substitution of 3  $O^{2-}$  by 2  $N^{3-}$  (eq 2)

$$\frac{N_d}{N_t} = \frac{O_{NB} + (1/2)O_B}{(3/2)O_B} \quad (2)$$

Table 1 presents the obtained experimental ratios of  $O_B/O_{NB}$  as well as  $N_d/N_t$  and compares them with the expected

**Table 1. Experimental and Theoretical Ratios of Lithium Phosphate Oxide and Oxynitride Glasses**

	$O_B/O_{NB}$	$N_d/N_t$	$(O_B/O_{NB})^{47}$ theoretical	$(N_d/N_t)^{49}$ theoretical
LiPON_0	0.42			
LiPON_50	0.33	2.39	0.29	2.32
LiPON_100	0.22	3.42	0.18	3.33

theoretical values for the analyzed samples found in the literature. As it can be observed, the values obtained from the theoretical models for a nitridated LiPON\_50 and LiPON\_100 films match well with the experimental ones, suggesting efficient nitrogen incorporation into the films for both cases.

A quasi-symmetrical peak was obtained in the P 2p photoelectron line for the three LiPON films, with no shape evolution upon nitridation (Figure 3). These peaks could be fitted with a main doublet, with spin-orbit splitting around 0.86 eV between  $2p_{3/2}$  and  $2p_{1/2}$  orbital lines. This doublet corresponds to the  $PO_4^{3-}$  tetrahedral environment present in the lithium phosphate. However, the binding energy shift observed for the different LiPON films is more pronounced than those found in the other elements ( $2p_{3/2}$  peaks located at  $134.1 > 133.0 > 132.5$  eV for LiPON\_0, LiPON\_50, and LiPON\_100, respectively) and it is believed to be nested on the replacement of P–O bonds by P–N bonds since reducing the average ionic charge on the phosphorus ions results in a decrease in the binding energy.<sup>26,47</sup>

Figure 4 shows the quantitative evolution of the O/P and N/P ratios with nitrogen incorporation. As it can be observed, the oxygen content decreases with the introduction of nitrogen (from 4.98 to 2.81 ratio) and vice versa in the case of nitrogen content (from 0 to 0.92). This matches well with the expected behavior: the O/P and N/P values obtained by Fleutot et al.<sup>26</sup>

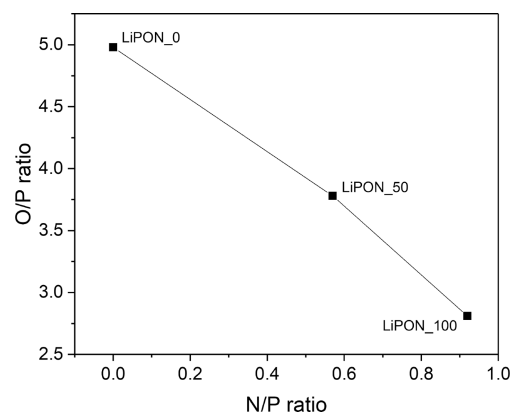


**Figure 4.** Quantitative evolution of O/P and N/P ratios with nitrogen incorporation.

range from 4.3 to 3.0 and from 0 to 1, respectively. Thus, this confirms the successful substitution of oxygen by nitrogen in the system, as discussed before.

Finally, looking back to Figure 3, similarly to the phosphorous case, the Li 1s spectra show a quasi-symmetrical shape. They are analyzed with a single lithium element, also undergoing a similar displacement observed in the previous cases,  $55.6 > 55.0 > 54.9$  eV for LiPON\_0, LiPON\_50, and LiPON\_100, respectively.

After characterizing the LiPON morphology and composition, the in-plane ionic conductivity of the thin films was measured by means of electrochemical impedance spectroscopy (EIS) using a two-probe method. Figure 5 shows the

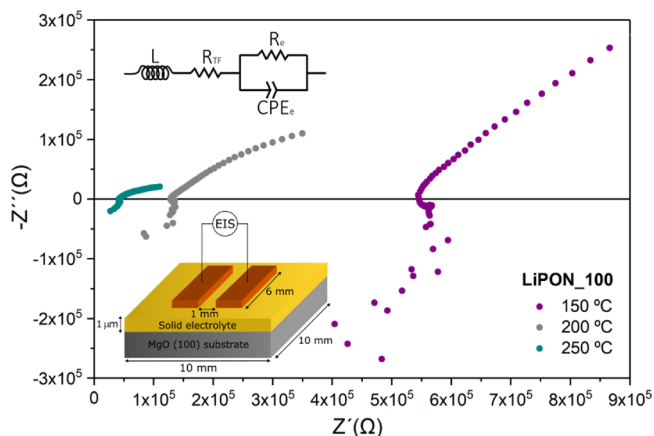


**Figure 5.** Obtained electrochemical impedance spectra of the LiPON\_100 thin-film electrolyte at 150, 200, and 250 °C along with the used equivalent circuit and the schematic illustration of the setup for the electrical measurement of the film samples.

schematic illustration of the experimental setup for the electrical measurement of the thin-film conductivity, including the dimensions and layout of the Cu contacts. Exemplifying Nyquist plots obtained for a LiPON\_100 film at different temperatures are also reproduced (the results obtained at 100 °C have not been graphed to show the other plots with better resolution). The corresponding equivalent circuit is shown in the figure inset, a setup-associated inductance ( $L$ ) was always observed at high frequencies followed by a resistive contribution ( $R_{TF}$ ), in series with an  $R_e$ – $CPE_e$  contribution at low frequencies. The setup-associated inductance is

displayed as negative  $Z''$  values that correspond to a high-frequency inductive response of the measurement system (electrometer and wires) that cannot be eliminated.<sup>50</sup> The series resistance  $R_{TF}$  is interpreted as the ohmic resistance associated with the  $\text{Li}^+$  conduction through the thin film, whereas the low-frequency contribution is associated with electrode-related phenomena. Moreover, note that the expected electronic resistance associated with contacts and cables, incorporated in the  $R_{TF}$  contribution, is much lower than that associated with the  $\text{Li}^+$  mobility and can thus be neglected.

The temperature dependence of the electrolyte resistivity is widely studied in the reported literature,<sup>51,52</sup> being a thermally activated conduction mechanism that follows the Arrhenius equation (eq 3)<sup>53</sup>

$$\sigma = \frac{\sigma_0}{T} e^{-E_a/kT} \quad (3)$$

where  $\sigma_0$  is the pre-exponential factor related to the number of charge carriers,  $T$  is the temperature in Kelvin,  $k$  is the Boltzmann constant, and  $E_a$  is the activation energy of the diffusion process.

Figure 6 presents the Arrhenius representation of the ionic conductivity calculated from the measured impedance at

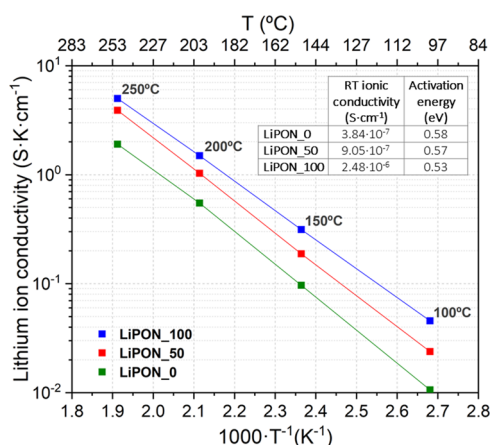


**Figure 6.** Arrhenius plots of ionic conductivity and activation energy at room temperature for samples LiPON\_0, LiPON\_50, and LiPON\_100.

different temperatures for the three samples under study. Two clear observations can be drawn from this figure. First, the ionic conductivity of LiPON significantly increases with the incorporation of nitrogen, reaching a maximum value of  $9.56 \times 10^{-2} \text{ S cm}^{-1}$  at 250 °C for the LiPON\_100 film. Second, the activation energy is slightly reduced, from 0.58 to 0.53 eV for the LiPON\_0 and 100, respectively. These results match well with previous observations in the literature since N substitution in the  $\text{Li}_3\text{PO}_4$  glass structure seems to reduce the non-bridging vs bridging P–O bond ratio, favoring the  $\text{Li}^+$  hopping through the LiPON network.<sup>26,54</sup> Also, from a processing perspective, the results suggest that a  $\text{N}_2$ -saturated background pressure during sputtering deposition is preferred for the incorporation of the optimum amount of N in the LiPON system. By extrapolating the ionic conductivity to room temperature (RT), the best-performing film, LiPON\_100, reaches a conductivity of  $2.48 \times 10^{-6} \text{ S cm}^{-1}$ , in good agreement with the literature (see, e.g., Bates and co-

workers, who measured  $\sim 2 \times 10^{-6} \text{ S cm}^{-1}$  at 25 °C in films deposited also by sputtering  $\text{Li}_3\text{PO}_4$  in pure  $\text{N}_2$ ).<sup>16</sup> These results validate, from a  $\text{Li}^+$ -ion mobility perspective, the use of LiPON\_100 as a solid electrolyte in this work.

**3.2. Anode Characterization.** The lithium films were deposited on SS substrates and presented a granulated and highly dense structure, as can be seen in Figure S3 of the SI. Moreover, the lithium surface roughness is induced by the morphology of the SS substrate. The elemental characterization of the as-deposited lithium surface was carried out using XPS. Figure 7 shows the survey spectrum, along with the

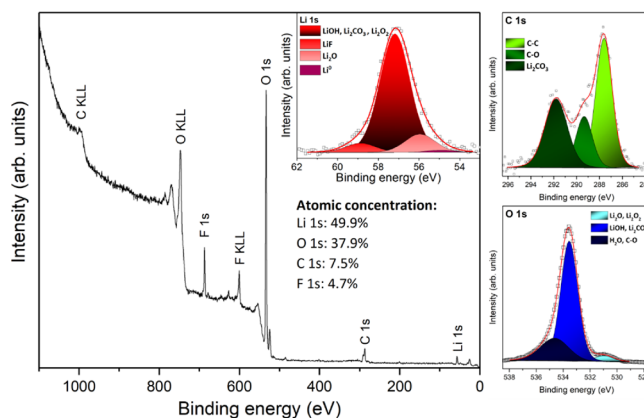


**Figure 7.** XPS survey spectra, Li 1s (inset graph), C 1s, and O 1s regions of the evaporated lithium deposited on the SS substrate (Mg  $K\alpha$  source). The normalized surface atomic concentration is also shown in the figure.

Li 1s, O 1s, and C 1s regions acquired with higher resolution. The atomic concentration values were calculated from the peak areas of each element in the survey spectrum, considering the corresponding relative sensitivity factors and the equipment transmission function. From obtained atomic concentration values, it can be concluded that the surface layer consists of lithium (49.9%), oxygen (37.9%) and, carbon (7.5%). Besides the adventitious carbon and surface oxides, some fluorine traces (4.7%) were also detected: most probably coming from the Viton gaskets used in the XPS chamber. According to the O 1s and C 1s regions, where  $\text{Li}_2\text{CO}_3$  and  $\text{Li}_2\text{O}/\text{Li}_2\text{O}_2$  components appear, it can be concluded that the as-deposited anode surface mainly consists of oxides and carbonates. Based on these deconvolutions, it is also possible to identify the different species that are usually overlapping in the Li 1s region, namely,  $\text{LiOH}$ ,  $\text{Li}_2\text{CO}_3$ ,  $\text{Li}_2\text{O}/\text{Li}_2\text{O}_2$ ,  $\text{LiF}$ , and to a significantly lesser extent  $\text{Li}^0$ . All these contaminants result from the reaction of Li with traces of  $\text{O}_2$ ,  $\text{CO}_2$ , F, and  $\text{H}_2\text{O}$  present in the process chamber even when not exposed to air.

The electrochemical performance of the LNMO//Li thin-film cell assembled with the conventional liquid electrolyte as a separator is added in the SI (Figure S4).

**3.3. Electrochemical Performance of the All-Solid-State Cell.** In Figure 8a, the ASSB stack is shown after deposition of all components, which can be clearly differentiated. Figure 8b shows the cross-sectional SEM image of the thin-film cell. The whole cathode/electrolyte/anode cell stack has a thickness below  $5 \mu\text{m}$ . This particular cross section image was obtained using silicon as the substrate due to its handling advantages in terms of ease of cleavage (note that this substrate is not the one used for functional ASSBs). A columnar layer of

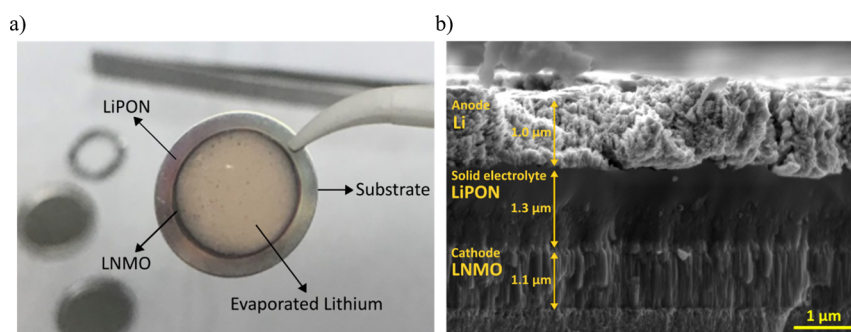


**Figure 8.** (a) Appearance of the ASSB full cell. Different layers can be identified depending on the diameter of the masks used to deposit them. (b) Cross-sectional SEM image of the battery stack deposited on a silicon substrate.

LNMO with an approximate thickness of  $1 \mu\text{m}$  and, on top of the latter, a smooth surface film of LiPON can be observed in Figure 8b. The good adhesion between the different defect-free and uniform thin films, with no evidence of any intermediate newly formed layer, can also be inferred from this figure. For the anode, a non-uniform surface was obtained. In addition, the Li thin film was covered with a titanium layer, deposited by DC magnetron sputtering, in order to avoid the interaction/degradation of Li metal under the SEM electron beam.

Figure 9 shows a diagram of the three cells with different anode structures analyzed in this work: LNMO/LiPON/Li

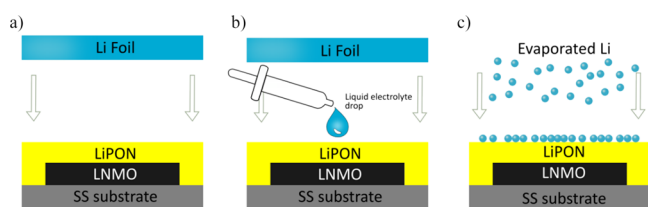


**Figure 9.** Schematic diagrams of the tested cell structures: (a) ASSB\_Foil, (b) ASSB\_Drop\_Foil, and (c) ASSB\_ThinFilm.

foil, LNMO/LiPON/Li foil + liquid electrolyte drop, and LNMO/LiPON/evaporated Li. They will be referred herein after as ASSB\_Foil, ASSB\_Drop\_Foil, and ASSB\_ThinFilm, respectively. It is important to note that considering the density and homogeneity of LiPON films (Figures 2 and 8 and Figure S1) along with the larger area of the LiPON film with respect to the LNMO one, the possibility of having direct contact of the liquid electrolyte with the LNMO is negligible.

Figure 10a shows the discharge specific capacity and the corresponding CE of ASSB\_Foil, ASSB\_Drop\_Foil, and ASSB\_ThinFilm at different C-rates (between 3.5 V vs  $\text{Li/Li}^+$ ). At C/20, the discharge specific capacity of ASSB\_Foil was  $33.0 \text{ mAh g}^{-1}$ , much lower than the other two samples. When the drop of liquid electrolyte is introduced, ASSB\_Drop\_Foil, the initial value at C/20 reached  $121.1 \text{ mAh g}^{-1}$ . However, this value decreases rapidly over the first 5 cycles at this C-rate, losing 52.9% of its initial value. This may be due to the irreversible reactions triggered by the liquid electrolyte that occur at the interlayers during the first few cycles, leading to the formation of an SEI in the Li anode as suggested by the electrochemical response of the LNMO//Li cell assembled with the liquid electrolyte and shown in Figure S4. This deterioration was not that evident in the case of the thin-film cell, ASSB\_ThinFilm, which in the fifth cycle only loses 15.6% of its initial value ( $80.5 \text{ mAh g}^{-1}$ ). At C/10, the highest discharge specific capacity value corresponds to ASSB\_ThinFilm,  $48.8 \text{ mAh g}^{-1}$ , better than the  $40.9$  and  $16.4 \text{ mAh g}^{-1}$  of ASSB\_Drop\_Foil and ASSB\_Foil, respectively. By increasing the C-rate to C/5, the ASSB\_ThinFilm, ASSB\_Drop\_Foil, and ASSB\_Foil cells retain 52.5, 51.8, and 25.0% of their capacities at C/10, respectively. The 85.2% is lost at C/2 in the thin-film case, the 89.3% in the lithium foil with drop case, and almost 100% in the lithium foil without drop case. Although in all three cells, the capacity is reduced down to zero at 1C, they recover 94.6, 52.9, and almost 100% (ASSB\_ThinFilm, ASSB\_Drop\_Foil, and ASSB\_Foil, respectively) of their initial specific discharge capacities upon cycling back to C/20 (note that these values were calculated based on the first cycle at C/

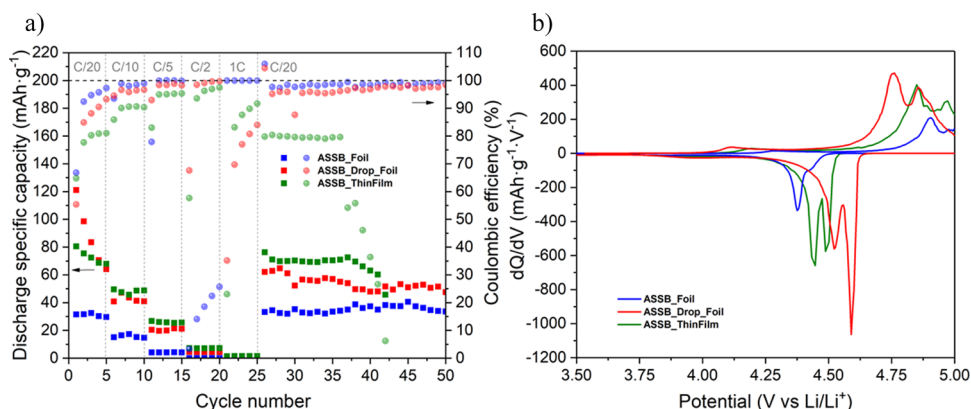


**Figure 10.** (a) Discharge specific capacity (filled squares) and corresponding Coulombic efficiency (filled circle) at different C-rates and (b)  $dQ/dV$  vs voltage curves derived from the charge/discharge cycle at C/20 of ASSB\_Foil, ASSB\_Drop\_Foil, and ASSB\_ThinFilm cells.

20). In the last long cycling at C/20, the discharge specific capacity values (ASSB\_ThinFilm > ASSB\_Drop\_Foil > ASSB\_Foil) remain relatively stable. As is can be seen, the liquid electrolyte drop enhances ion diffusion between the lithium foil and the LiPON. Even so, the result can be improved by using evaporated lithium. Unfortunately, in cycle 37, the ASSB\_ThinFilm begins to lose the specific discharge capacity, short-circuiting the battery. The formation of lithium dendrites may be the cause of this deterioration.

Regarding the CE, rather low values were obtained in the first cycle, particularly in the case of the ASSB\_Drop\_Foil (55.4%, versus 64.8 and 66.8% of ASSB\_ThinFilm and ASSB\_Foil, respectively). This is ascribed to the liquid electrolyte decomposition process in the anode interface at high voltages occurring predominantly during the charge.<sup>55</sup> The first cycle has been included in the SI. The LiPON, besides its role as a solid electrolyte, also acts as a cathode protector.<sup>31,32</sup> For the rest of the cycle, ASSB\_Foil shows a CE of 97.3% in the last cycle at C/20, exceeding 98% at C/10 and reaching almost 100% at C/5. ASSB\_Drop\_Foil was below 94% in the last cycle at C/20, while the CE was 96.6 and 98.8% at C/10 and C/5, respectively. Furthermore, higher CE values for the ASSB\_Foil than for the ASSB\_Drop\_Foil were observed during long cycling at C/20: 98.9 and 97.3%, respectively. In the case of ASSB\_ThinFilm, the CE remains below the other two cells, up to 81.0% during the initial cycling stage at C/20, reaching a maximum value of 97.4% at high C-rates (C/2) and around 80% during the last long cycling at C/20. A possible explanation for the pronounced difference observed in the CE may likely rely on the high reactivity of the evaporated lithium with the solid electrolyte; in addition, more unwanted reactions are expected for ASSB\_ThinFilm cells than for ASSB\_Foil cells due to the high surface-to-volume ratio, typical of thin-film electrodes.

The ASSB\_ThinFilm cell electrochemical performance is limited, particularly if it is compared with a previous report of the same cell grown by RF sputtering on Pt-coated Al<sub>2</sub>O<sub>3</sub> substrates.<sup>6</sup> In this case, the cell delivered a first cycle capacity of 122 mAh g<sup>-1</sup> at C/10 and a 90.6% capacity retention after 10,000 cycles and a 99.98% Coulombic efficiency. During the revision process of this work, another report on thin-film LNMO/LiPON/Li cells grown by pulsed laser deposition (PLD) on Pt-coated Al<sub>2</sub>O<sub>3</sub> substrates was published.<sup>56</sup> This work presented a cell that delivered 99.6% Coulombic efficiency after 600 cycles; however, the reported capacity values of the cell were not very high: ~18 μAh cm<sup>-2</sup> μm<sup>-1</sup> as normalized to the cathode thickness, three times lower than the capacity of our cathode (65 μAh cm<sup>-2</sup> μm<sup>-1</sup>).<sup>57</sup> In any case, it is worth mentioning that those two reports on thin-film LNMO/LiPON/Li cells present results of batteries that have been grown on Pt-coated Al<sub>2</sub>O<sub>3</sub> substrates, with the Pt cost at \$28,000 kg<sup>-1</sup>, using evaporation techniques, namely, RF magnetron sputtering and PLD, which involve a much higher production cost than the ones used in this work.

In order to analyze the redox reactions and voltage hysteresis between the charge and discharge of the battery, differential capacity curves (dQ/dV) were used (Figure 10b). In all three cells, during charge (from 3.5 to 5 V vs Li/Li<sup>+</sup>) and discharge (from 5 to 3.5 V vs Li/Li<sup>+</sup>), two high-voltage transitions can be distinguished related to the successive oxidation of Ni<sup>2+</sup> to Ni<sup>3+</sup> and Ni<sup>4+</sup>. In addition, another capacity contribution corresponding to the presence of Mn<sup>3+</sup> (redox pair Mn<sup>3+</sup>/Mn<sup>4+</sup>) at around 4 V vs Li/Li<sup>+</sup> is also revealed, particularly in the

ASSB\_Drop\_Foil cell. In the case of ASSB\_Foil, the nickel-related redox peaks appear during the charge at 4.90 and 4.97 V vs Li/Li<sup>+</sup> (Ni<sup>2+/3+</sup> and Ni<sup>3+/4+</sup>, respectively), while, during discharge, they appear at 4.37 and 4.43 V vs Li/Li<sup>+</sup>, the second transition being less pronounced than the first one. This voltage difference leads to a hysteresis of 0.53 V, higher than in the other two cells: 0.26 V for the ASSB\_Drop\_Foil cell and 0.39 V for the ASSB\_ThinFilm cell. These results prove that the liquid electrolyte drop at the interface between the Li foil anode and LiPON electrolyte can effectively weaken the polarization during charge and discharge, most probably due to an improvement of the lithium-ion migration. Importantly, the evaporated lithium reduces this polarization without the need of introducing any liquid component, thus improving battery safety.

For a better analysis of the internal resistance, an EIS study was carried out. The data were collected in the 100 mHz–7 MHz frequency range once the cell was assembled. Figure 11

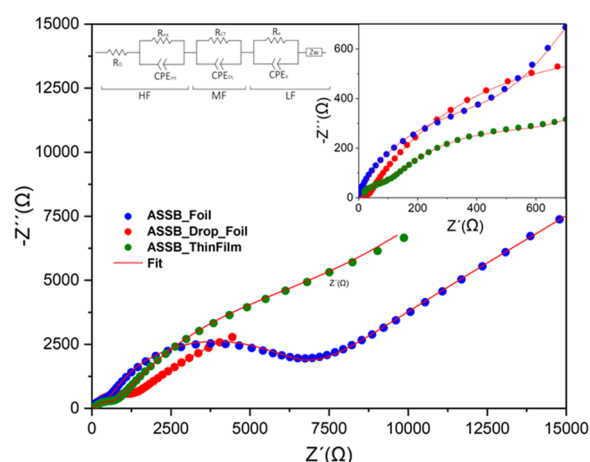


**Figure 11.** Nyquist plots of ASSB\_Foil, ASSB\_Drop\_Foil, and ASSB\_ThinFilm along with the equivalent circuit and the fitted data.

shows the Nyquist plots of ASSB\_Foil, ASSB\_Drop\_Foil, and ASSB\_ThinFilm cells fitted with the proposed equivalent circuit (see inset drawing). For the sake of clarity, the zoomed graph is included in the right-inset graph. The impedance curves show a semicircle at a high frequency (HF) followed by a more prominent semicircle at mid frequency (MF) and ending with a semicircular tail at low frequency (LF). A possible explanation of the equivalent circuit could be as follows: the HF contribution is originated by the  $R_{\text{int}}-CPE_{\text{int}}$  contribution of interfacial layers in series with the electrolyte ohmic resistance ( $R_{\Omega}$ ), corresponding to the Li<sup>+</sup> resistance across the electrolyte (the expected electronic resistance associated with contacts and cables was neglected). The semicircle at MF is ascribed to a charge-transfer resistance and a double-layer capacitance ( $R_{\text{CT}}-CPE_{\text{DL}}$ ), both connected in parallel. Finally, the LF range is ascribed to an RC semicircle associated with bulk electronic resistance ( $R_e$ ) and charge accumulation capacitance ( $CPE_e$ ) along with the Warburg diffusion element ( $Z_w$ ) that accounts for the sloping line ascribed to the solid-state diffusion of Li<sup>+</sup> in the crystal. Table 2 presents the fitted values for the high-frequency part, which is the one ascribed to the interface processes. Since different samples are involved, the results have been normalized concerning the area for resistance (area-specific resistance, ASR) in Ω cm<sup>2</sup> and capacity in F cm.



**Table 2. Values Corresponding to the Interfacial Layer ( $R_{\text{int}}-C_{\text{int}}$ ) Contribution, Charge-Transfer Resistance and a Double-Layer Capacitance ( $R_{\text{CT}}-C_{\text{DL}}$ ), and Respective Time Constants ( $\tau = RC$ )**

	ASSB_Foil	ASSB_Drop_Foil	ASSB_ThinFilm
$R_{\text{int}}$ ( $\Omega \text{ cm}^2$ )	530	30	105
$C_{\text{int}}$ ( $\text{F cm}^{-2}$ )	$3.2 \times 10^{-9}$	$2.6 \times 10^{-8}$	$1.1 \times 10^{-8}$
$\tau_{\text{int}}$ (s)	$1.7 \times 10^{-6}$	$7.8 \times 10^{-7}$	$1.2 \times 10^{-6}$
$R_{\text{CT}}$ ( $\Omega \text{ cm}^2$ )	6,198	1,070	697
$C_{\text{DL}}$ ( $\text{F cm}^{-2}$ )	$2.8 \times 10^{-8}$	$4.3 \times 10^{-6}$	$1.8 \times 10^{-7}$
$\tau_{\text{CT-DL}}$ (s)	$1.7 \times 10^{-4}$	$4.6 \times 10^{-3}$	$1.3 \times 10^{-4}$

The different RC contributions of the three cells could be compared considering the value of  $\tau$ . In the first contribution, the three samples are roughly of the same order of magnitude ( $10^{-6}$ ), suggesting that they correspond to the same interfacial feature. Particularly, they refer to the formation of a passivating layer on the electrode/electrolyte interface. The value of the resistance ( $R_{\text{int}}$ ) follows this trend for the different cells: ASSB\_Drop\_Foil < ASSB\_ThinFilm  $\ll$  ASSB\_Foil. In the ASSB\_Foil cell, the poor contact between the lithium and the solid electrolyte makes the formation of the SEI layer between them highly resistive. By improving the contact by adding a liquid electrolyte, the  $R_{\text{int}}$  was reduced to  $30 \Omega \text{ cm}^2$ , resulting in a significant improvement of the SEI. The ASSB\_ThinFilm cell achieved an intermediate resistance, exactly  $105 \Omega \text{ cm}^2$ . The interfacial reactions between the evaporated lithium anode and the solid electrolyte seem to be more active than those corresponding to the lithium foil. This high reactivity, and the absence of contaminating species that are typically present on the surface of commercial lithium foil, helps the formation of a better SEI, thus improving contact.

The  $\tau$  of the second semicircle also coincides in all three samples ( $\sim 10^{-4}$  s). Interestingly, a lower charge-transfer resistance was obtained in the case of the evaporated lithium,  $698 \Omega \text{ cm}^2$  vs  $1,070$  and  $6,199 \Omega \text{ cm}^2$  for ASSB\_Drop\_Foil and ASSB\_Foil cells, respectively. This improvement in the pass through of Li ions could be caused by a larger contact surface. The fact that lithium is deposited directly on the LiPON surface, without the need to introduce a bonding medium, results in a more active area. The higher resistance of the ASSB\_Drop cell may also be due to the fact that there are two media through which the Li must pass (two charge transfers; from Li ions to liquid and from liquid to LiPON). In the case of ASSB\_Foil, the roughness and stiffness of the Li foil make the active surface smaller, which would be behind the highest charge-transfer resistance observed.

For a better interpretation, Figure 12 shows a schematic representation of the anode/electrolyte interface of ASSB\_Foil, ASSB\_Drop\_Foil, and ASSB\_ThinFilm cells. In the ASSB\_Foil case, where the lithium foil is placed directly on top of the solid electrolyte, the Li-ion diffusion paths are limited by the

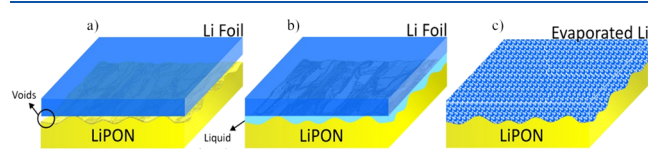


**Figure 12.** Schematic illustration of the anode/solid electrolyte interface of (a) ASSB\_Foil, (b) ASSB\_Drop\_Foil, and (c) ASSB\_ThinFilm.

voids created in the interface due to the poor adhesion between the Li foil and the LiPON.<sup>37</sup> When a drop of liquid electrolyte is added, the voids are filled, improving their contact although adding an extra media for the Li to cross. For the ASSB\_ThinFilm cell, the lithium was evaporated, avoiding possible voids due to the adaptation of the lithium atoms to the roughness of the LiPON.

Finally, to validate the successful implementation of the monolithic high-voltage all-solid-state thin-film battery deposited layer by layer, a series of voltage tests were performed. Figure S7b of the Supporting Information shows the nominal voltage of the assembled high-voltage pouch cell delivering 4.72 V. Moreover, the cell was able to light two 2.1 V forward voltage red LEDs arranged in series (Figure S7c of the Supporting Information). This is something that cannot be done with a conventional Li-ion battery as shown in the comparative experiment shown in the movie uploaded as a web-enhanced object where the lighting of the two 2.1 V red LEDs was attempted by a commercial Li-ion battery and our high-voltage battery (Video S1).

#### 4. CONCLUSIONS

In this work, a functional high-voltage, all-solid-state thin-film lithium-ion battery composed of LNMO as the cathode, LiPON as the solid electrolyte, and an evaporated lithium anode has been deposited layer by layer on a low-cost stainless-steel current collector. At  $\$1.5 \text{ kg}^{-1}$ , the cost of stainless steel is five times lower than Cu at  $\$8 \text{ kg}^{-1}$  and three orders of magnitude lower than Pt at  $\sim \$28,000 \text{ kg}^{-1}$ . Considering that stainless steel is already commercially available in  $>20 \mu\text{m}$ -thick foils, there can be a great saving with respect to conventional cells using Cu as the current collector or other thin-film cells that rely on  $0.65 \mu\text{m}$ -thick Pt layers, which have to be supported on an additional substrate. In terms of processing techniques, the AC magnetron sputtering technique used for the cathode growth is an effective physical vapor deposition technique that has several advantages over its RF magnetron sputtering counterpart. Besides improving process stability and increasing deposition rates, it is a processing technique that is used at lower power levels, with a low degree of technical complexity, hence resulting in a cost-effective processing method. The main cost difference is found on the power supply, which can range from  $\$4,000$  for a 10 kW AC power supply to  $\$3,000$  for a 600 W RF power supply, again several orders of magnitude difference in favor of AC magnetron sputtering, which needs lower maintenance and can reach deposition rates on oxide materials up to  $100 \text{ nm min}^{-1}$ , while RF magnetron sputtering yields deposition rates of  $1 \text{ nm min}^{-1}$ . Altogether, it represents a considerable cost reduction when using AC magnetron sputtering.

Before assembling the cells, each electroactive component of the battery has been characterized separately. All the deposited LiPON samples show smooth and highly dense structures with no signs of crystallization. The high impedance at RT evidenced the need for higher temperatures for a proper analysis of the LiPON ionic conductivity by means of the Arrhenius equation. The ionic conductivity increased with the temperature, being higher in samples deposited with a larger nitrogen percentage. As a result, the higher ionic conductivity at RT of  $2.48 \times 10^{-6} \text{ S cm}^{-1}$  corresponds to the  $\text{N}_2$ -saturated sputtering process, in good accordance with the literature. Moreover, the XPS shows a broad signal that can be resolved with  $\text{N}_a$  and  $\text{N}_t$  components and the analysis matches well with

the proposed O-substitution theoretical models, suggesting efficient nitrogen incorporation. All in all, this indicates that a N<sub>2</sub>-saturated background pressure is preferred for the incorporation of the optimum amount of N in the LiPON solid electrolyte system. Lithium anode thin films of approx. 1 μm were prepared by thermal evaporation on a stainless-steel substrate. The deposited lithium thin films presented a granulated and highly dense structure, with a substrate-induced roughness. Because of the high reactivity of the evaporated lithium, the surface mainly consists of oxides and carbonate species. Finally, the build-up of a high-voltage all-solid-state thin-film battery by combining the optimized functional films (electrode and electrolyte) was performed, sequentially depositing on a stainless-steel substrate.

To validate the successful implementation of the thin-film battery, a comparison of the electrochemical performance of the microbattery using evaporated lithium as well as lithium foil (commonly employed) was done. The lack of contact between the lithium foil and the LiPON limits the diffusion of ions between the anode and the electrolyte, thereby impairing the electrochemical performance of the cell. The addition of a liquid electrolyte drop provides a homogeneous interface, reaching 121.12 mAh g<sup>-1</sup> at C/20. The reduced cycle life of the evaporated lithium cell could have its origin in the Li film that presents a rougher morphology than the LNMO and LiPON layers. The low Coulombic efficiency, between 80 and 95%, of the evaporated lithium cell, in contrast with the higher values in the 95–99.9% range observed for the Li foil cell, is ascribed to interface reactions between LiPON and evaporated Li, which is highly reactive on its atomic form while being helped by the typically enhanced high surface-to-volume ratio of thin films. In any case, the evaporated lithium cells reach a higher specific capacity after 25 cycles, >70 mAh g<sup>-1</sup>, for the evaporated Li cell, in contrast with the values below 60 mAh g<sup>-1</sup> when using Li foil plus liquid electrolyte and the values below 40 mAh g<sup>-1</sup> when using Li foil. These results indicate a significant progress in the good direction toward the consecution of a commercial high-voltage thin-film battery supported on low-cost and abundant stainless-steel substrates.

## ■ ASSOCIATED CONTENT

### SI Supporting Information

The Supporting Information is available free of charge at <https://pubs.acs.org/doi/10.1021/acsaem.2c01581>.

(Section S1) Top-view SEM images of LiPON thin films deposited with different Ar-N<sub>2</sub> content, (Section S2) partial structure of nitride Li<sub>3</sub>PO<sub>4</sub> thin film, (Section S3) SEM images of the evaporated lithium on the SS substrate sample, (Section S4) C-rate of the LNMO//Li thin film cell assembled with the conventional liquid electrolyte as a separator, (Section S5) EDS mapping of the ASSB, (Section S6) initial cycle and differential capacity curves of the ASSB cells, and (Section S7) ASSB encapsulation system and validation (PDF)

Lighting of red LEDs using a commercial Li-ion battery and the high-voltage battery in the study (AVI)

## ■ AUTHOR INFORMATION

### Corresponding Author

Miguel Ángel Muñoz-Márquez – Centre for Cooperative Research on Alternative Energies (CIC energiGUNE), Basque Research and Technology Alliance (BRTA), 01510 Vitoria-

Gasteiz, Spain; Present Address: School of Science and Technology – Chemistry Division, University of Camerino, Via Madonna delle Carceri, 62032 Camerino, Italy.; [orcid.org/0000-0002-5351-828X](https://orcid.org/0000-0002-5351-828X); Email: [miguel.munoz@unicam.it](mailto:miguel.munoz@unicam.it)

## Authors

Íñaki Madinabeitia – TECNALIA, Basque Research and Technology Alliance (BRTA), Parque Científico y Tecnológico de Gipuzkoa, 20009 Donostia-San Sebastián, Spain; Centre for Cooperative Research on Alternative Energies (CIC energiGUNE), Basque Research and Technology Alliance (BRTA), 01510 Vitoria-Gasteiz, Spain; Departamento de Física de la Materia Condensada, Facultad de Ciencia y Tecnología, Universidad del País Vasco, UPV/EHU, 48080 Bilbao, Spain; [orcid.org/0000-0003-1896-9365](https://orcid.org/0000-0003-1896-9365)

Jokin Rikarte – Centre for Cooperative Research on Alternative Energies (CIC energiGUNE), Basque Research and Technology Alliance (BRTA), 01510 Vitoria-Gasteiz, Spain; Departamento de Física de la Materia Condensada, Facultad de Ciencia y Tecnología, Universidad del País Vasco, UPV/EHU, 48080 Bilbao, Spain; [orcid.org/0000-0003-2403-1568](https://orcid.org/0000-0003-2403-1568)

Ane Etxebarria – Centre for Cooperative Research on Alternative Energies (CIC energiGUNE), Basque Research and Technology Alliance (BRTA), 01510 Vitoria-Gasteiz, Spain; Departamento de Física de la Materia Condensada, Facultad de Ciencia y Tecnología, Universidad del País Vasco, UPV/EHU, 48080 Bilbao, Spain; Present Address: Interface Science Department. Fritz Haber Institute of the Max Planck Society, Faradayweg 4-6, 14195 Berlin, Germany.

Giorgio Baraldi – Centre for Cooperative Research on Alternative Energies (CIC energiGUNE), Basque Research and Technology Alliance (BRTA), 01510 Vitoria-Gasteiz, Spain; Present Address: IDETEC, Basque Research and Technology Alliance (BRTA), Parque Científico y Tecnológico de Gipuzkoa, Miramon Pasealekua 196, 20014 Donostia-San Sebastián, Spain

Francisco José Fernández-Carretero – TECNALIA, Basque Research and Technology Alliance (BRTA), Parque Científico y Tecnológico de Gipuzkoa, 20009 Donostia-San Sebastián, Spain

Íñigo Garbayo – Centre for Cooperative Research on Alternative Energies (CIC energiGUNE), Basque Research and Technology Alliance (BRTA), 01510 Vitoria-Gasteiz, Spain; Present Address: CENER (National Renewable Energy Centre), Av. Ciudad de la Innovación 7, 31621 Sarriguren, Spain.; [orcid.org/0000-0003-2494-173X](https://orcid.org/0000-0003-2494-173X)

Rosalía Cid – Centre for Cooperative Research on Alternative Energies (CIC energiGUNE), Basque Research and Technology Alliance (BRTA), 01510 Vitoria-Gasteiz, Spain; [orcid.org/0000-0001-7440-2932](https://orcid.org/0000-0001-7440-2932)

Alberto García-Luis – TECNALIA, Basque Research and Technology Alliance (BRTA), Parque Científico y Tecnológico de Gipuzkoa, 20009 Donostia-San Sebastián, Spain; [orcid.org/0000-0001-7541-3203](https://orcid.org/0000-0001-7541-3203)

Complete contact information is available at: <https://pubs.acs.org/doi/10.1021/acsaem.2c01581>

## Author Contributions

The manuscript was written through contributions of all authors. All authors have given approval to the final version of the manuscript.

## Notes

The authors declare no competing financial interest.

## ACKNOWLEDGMENTS

Victor Bellido-Gonzalez from Gencoa Ltd. (U.K.) is acknowledged for his comments and suggestions. The authors acknowledge the financial support from European H2020 project MONBASA (Monolithic Batteries for Spaceship Applications, grant no. 687561) and Basque Government through Elkartek 2017 program with the project Elkartek CICe2017-L4.

## REFERENCES

- (1) Armand, M.; Tarascon, J.-M. Building Better Batteries. *Nature* **2008**, *451*, 652–657.
- (2) Qian, G.; Liao, X.; Zhu, Y.; Pan, F.; Chen, X.; Yang, Y. Designing Flexible Lithium-Ion Batteries by Structural Engineering. *ACS Energy Lett.* **2019**, *4*, 690–701.
- (3) Xia, S.; Wu, X.; Zhang, Z.; Cui, Y.; Liu, W. Practical Challenges and Future Perspectives of All-Solid-State Lithium-Metal Batteries. *Chem* **2019**, *5*, 753–785.
- (4) Jiang, Z.; Han, Q.; Wang, S.; Wang, H. Reducing the Interfacial Resistance in All-Solid-State Lithium Batteries Based on Oxide Ceramic Electrolytes. *ChemElectroChem* **2019**, *6*, 2970–2983.
- (5) Janek, J.; Zeier, W. G. A Solid Future for Battery Development. *Nat. Energy* **2016**, *1*, 1–4.
- (6) Li, J.; Ma, C.; Chi, M.; Liang, C.; Dudney, N. J. Solid Electrolyte: The Key for High-Voltage Lithium Batteries. *Adv. Energy Mater.* **2015**, *5*, 1401408.
- (7) Dudney, N. J.; Neudecker, B. J. Solid State Thin-Film Lithium Battery Systems. *Curr. Opin. Solid State Mater. Sci.* **1999**, *4*, 479–482.
- (8) Dudney, N. J. Thin Film Micro-Batteries. *Electrochem. Soc. Interface* **2008**, *17*, 44–48.
- (9) Bates, J. B.; Gruzalski, G. R.; Dudney, N. J.; Luck, C. F.; Yu, X. Rechargeable Thin-Film Lithium Batteries. *Solid State Ionics* **1994**, *70-71*, 619–628.
- (10) Arnell, R. D.; Kelly, P. J. Recent Advances in Magnetron Sputtering. *Surf. Coat. Technol.* **1999**, *112*, 170–176.
- (11) Swann, S. Magnetron Sputtering. *Phys. Technol.* **1988**, *19*, 67–75.
- (12) Safi, I. Recent Aspects Concerning DC Reactive Magnetron Sputtering of Thin Films: A Review. *Surf. Coat. Technol.* **2000**, *127*, 203–218.
- (13) Jayanth Babu, K.; Jeevan Kumar, P.; Hussain, O. M. Microstructural and Electrochemical Properties of Rf-Sputtered  $\text{LiMn}_2\text{O}_4$  Thin Film Cathodes. *Appl. Nanosci. (Switzerland)* **2012**, *2*, 401–407.
- (14) Julien, C. M.; Mauger, A.; Hussain, O. M. Sputtered  $\text{LiCoO}_2$  Cathode Materials for All-Solid-State Thin-Film Lithium Micro-batteries. *Materials* **2019**, *12*, 1–26.
- (15) Sugiawati, V. A.; Vacandio, F.; Perrin-Pellegrino, C.; Galeyeva, A.; Kurbatov, A. P.; Djenzian, T. Sputtered Porous Li-Fe-P-O Film Cathodes Prepared by Radio Frequency Sputtering for Li-Ion Microbatteries. *Sci. Rep.* **2019**, *9*, 11172.
- (16) Bates, J. B.; Dudney, N. J.; Gruzalski, G. R.; Zuhr, R. A.; Choudhury, A.; Luck, C. F.; Robertson, J. D. Fabrication and Characterization of Amorphous Lithium Electrolyte Thin Films and Rechargeable Thin-Film Batteries. *J. Power Sources* **1993**, *43*, 103–110.
- (17) Lobe, S.; Dellen, C.; Finsterbusch, M.; Gehrke, H. G.; Sebold, D.; Tsai, C. L.; Uhlenbruck, S.; Guillon, O. Radio Frequency Magnetron Sputtering of  $\text{Li}_7\text{La}_3\text{Zr}_2\text{O}_{12}$  Thin Films for Solid-State Batteries. *J. Power Sources* **2016**, *307*, 684–689.
- (18) Kumatani, A.; Shiraki, S.; Takagi, Y.; Suzuki, T.; Ohsawa, T.; Gao, X.; Ikuhara, Y.; Hitosugi, T. Epitaxial Growth of  $\text{Li}_4\text{Ti}_5\text{O}_{12}$  Thin Films Using RF Magnetron Sputtering. *Jpn. J. Appl. Phys.* **2014**, *53*, 058001.
- (19) Lee, W. H.; Son, H. C.; Moon, H. S.; Kim, Y. I.; Sung, S. H.; Kim, J. Y.; Lee, J. G.; Park, J. W. Stoichiometry Dependence of Electrochemical Performance of Thin-Film  $\text{SnO}_x$  Microbattery Anodes Deposited by Radio Frequency Magnetron Sputtering. *J. Power Sources* **2000**, *89*, 102–105.
- (20) Tan, X. Q.; Liu, J. Y.; Niu, J. R.; Liu, J. Y.; Tian, J. Y. Recent Progress in Magnetron Sputtering Technology Used on Fabrics. *Materials* **2018**, *11*, 1953.
- (21) Oleshko, V. P.; Lam, T.; Ruzmetov, D.; Haney, P.; Lezec, H. J.; Davydov, A. V.; Krylyuk, S.; Cumings, J.; Talin, A. A. Miniature All-Solid-State Heterostructure Nanowire Li-Ion Batteries as a Tool for Engineering and Structural Diagnostics of Nanoscale Electrochemical Processes. *Nanoscale* **2014**, *6*, 11756–11768.
- (22) Christiansen, A. S.; Stamate, E.; Thydén, K.; Younesi, R.; Holtappels, P. Plasma Properties during Magnetron Sputtering of Lithium Phosphorous Oxynitride Thin Films. *J. Power Sources* **2015**, *273*, 863–872.
- (23) Dudney, N. J. Addition of a Thin-Film Inorganic Solid Electrolyte (Lipon) as a Protective Film in Lithium Batteries with a Liquid Electrolyte. *J. Power Sources* **2000**, *89*, 176–179.
- (24) Choi, C. H.; Cho, W. I.; Cho, B. W.; Kim, H. S.; Yoon, Y. S.; Tak, Y. S. Radio-Frequency Magnetron Sputtering Power Effect on the Ionic Conductivities of Lipon Films. *Electrochem. Solid-State Lett.* **2002**, *5*, A14–A17.
- (25) Park, H. Y.; Nam, S. C.; Lim, Y. C.; Choi, K. G.; Lee, K. C.; Park, G. B.; Lee, S. R.; Kim, H. P.; Cho, S. B. Effects of Sputtering Pressure on the Characteristics of Lithium Ion Conductive Lithium Phosphorous Oxynitride Thin Film. *J. Electroceram.* **2006**, *17*, 1023–1030.
- (26) Fleutot, B.; Pecquenard, B.; Martinez, H.; Letellier, M.; Levasseur, A. Investigation of the Local Structure of LiPON Thin Films to Better Understand the Role of Nitrogen on Their Performance. *Solid State Ionics* **2011**, *186*, 29–36.
- (27) Schilcher, C.; Meyer, C.; Kwade, A. Structural and Electrochemical Properties of Calendered Lithium Manganese Oxide Cathodes. *Energy Technol.* **2016**, *4*, 1604–1610.
- (28) Liu, D.; Zhu, W.; Trottier, J.; Gagnon, C.; Barray, F.; Guerfi, A.; Mauger, A.; Groult, H.; Julien, C. M.; Goodenough, J. B.; Zaghbi, K. Spinel Materials for High-Voltage Cathodes in Li-Ion Batteries. *RSC Adv.* **2014**, *4*, 154–167.
- (29) Yi, T. F.; Mei, J.; Zhu, Y. R. Key Strategies for Enhancing the Cycling Stability and Rate Capacity of  $\text{LiNi}_{0.5}\text{Mn}_{1.5}\text{O}_4$  as High-Voltage Cathode Materials for High Power Lithium-Ion Batteries. *J. Power Sources* **2016**, *316*, 85–105.
- (30) Fang, X.; Ge, M.; Rong, J.; Che, Y.; Aroonyadet, N.; Wang, X.; Liu, Y.; Zhang, A.; Zhou, C. Ultrathin Surface Modification by Atomic Layer Deposition on High Voltage Cathode  $\text{LiNi}_{0.5}\text{Mn}_{1.5}\text{O}_4$  for Lithium Ion Batteries. *Energy Technol.* **2014**, *2*, 159–165.
- (31) Baggetto, L.; Unocic, R. R.; Dudney, N. J.; Veith, G. M. Fabrication and Characterization of Li–Mn–Ni–O Sputtered Thin Film High Voltage Cathodes for Li-Ion Batteries. *J. Power Sources* **2012**, *211*, 108–118.
- (32) Kim, Y.; Dudney, N. J.; Chi, M.; Martha, S. K.; Nanda, J.; Veith, G. M.; Liang, C. A Perspective on Coatings to Stabilize High-Voltage Cathodes:  $\text{LiMn}_{1.5}\text{Ni}_{0.5}\text{O}_4$  with Sub-Nanometer Lipon Cycled with  $\text{LiPF}_6$  Electrolyte. *J. Electrochem. Soc.* **2013**, *160*, A3113–A3125.
- (33) Baggetto, L.; Dudney, N. J.; Veith, G. M. Surface Chemistry of Metal Oxide Coated Lithium Manganese Nickel Oxide Thin Film Cathodes Studied by XPS. *Electrochim. Acta* **2013**, *90*, 135–147.
- (34) Shiraki, S.; Kawasoko, H.; Suzuki, T.; Shimizu, R.; Hitosugi, T. Very-Low Solid-Electrolyte/Electrode Interface Resistance in  $\text{Li}(\text{Ni}_{0.5}\text{Mn}_{1.5})\text{O}_4$ -Based Thin-Film Lithium Battery. *ECS Meet. Abstr.* **2016**, *MA2016-02*, 294.

(35) West, W. C.; Whitacre, J. F.; Ratnakumar, B. V. Radio Frequency Magnetron-Sputtered  $\text{LiCoPO}_4$  Cathodes for 4.8 V Thin-Film Batteries. *J. Electrochem. Soc.* **2003**, *150*, A1660.

(36) Albertus, P.; Anandan, V.; Ban, C.; Balsara, N.; Belharouak, I.; Buettner-Garrett, J.; Chen, Z.; Daniel, C.; Doeff, M.; Dudney, N. J.; Dunn, B.; Harris, S. J.; Herle, S.; Herbert, E.; Kalnaus, S.; Libera, J. A.; Lu, D.; Martin, S.; McCloskey, B. D.; McDowell, M. T.; Meng, Y. S.; Nanda, J.; Sakamoto, J.; Self, E. C.; Tepavcevic, S.; Wachsman, E.; Wang, C.; Westover, A. S.; Xiao, J.; Yersak, T. Challenges for and Pathways toward Li-Metal-Based All-Solid-State Batteries. *ACS Energy Lett.* **2021**, *6*, 1399–1404.

(37) Kim, J. H.; Xiao, C.-F.; Han, J.; Kim, Y. J.; Yagi, S.; Kim, H.-S. Interface Control for High-Performance All-Solid-State Li Thin-Film Batteries. *Ceram. Int.* **2020**, *46*, 9960–19965.

(38) Schwöbel, A.; Hausbrand, R.; Jaegermann, W. Interface Reactions between LiPON and Lithium Studied by In-Situ X-Ray Photoemission. *Solid State Ionics* **2015**, *273*, 51–54.

(39) Kawasoko, H.; Shiraki, S.; Suzuki, T.; Shimizu, R.; Hitosugi, T. Extremely Low Resistance of  $\text{Li}_3\text{PO}_4$  Electrolyte/ $\text{Li}(\text{Ni}_{0.5}\text{Mn}_{1.5})\text{O}_4$  Electrode Interfaces. *ACS Appl. Mater. Interfaces* **2018**, *10*, 27498–27502.

(40) Madinabeitia, I.; Rikarte, J.; Baraldi, G.; Fernández-Carretero, F. J.; Garbayo, I.; García-Luis, A.; Muñoz-Márquez, M. Á. Growth Parameters and Diffusion Barriers for Functional High-Voltage Thin-Film Batteries Based on Spinel  $\text{LiNi}_{0.5}\text{Mn}_{1.5}\text{O}_4$  Cathodes. *ACS Appl. Mater. Interfaces* **2022**, *14*, 2720–2730.

(41) Nimisha, C. S.; Rao, K. Y.; Venkatesh, G.; Rao, G. M.; Munichandraiah, N. Sputter Deposited LiPON Thin Films from Powder Target as Electrolyte for Thin Film Battery Applications. *Thin Solid Films* **2011**, *519*, 3401–3406.

(42) Hu, Z.; Li, D.; Xie, K. Influence of Radio Frequency Power on Structure and Ionic Conductivity of LiPON Thin Films. *Bull. Mater. Sci.* **2008**, *31*, 681–686.

(43) Cantín, A.; Corma, A.; Diaz-Cabanas, M. J.; Jordá, J. L.; Moliner, M. Rational Design and HT Techniques Allow the Synthesis of New IWR Zeolite Polymorphs. *J. Am. Chem. Soc.* **2006**, *128*, 4216–4217.

(44) Su, Y.; Falgenhauer, J.; Polity, A.; Leichtweiß, T.; Kronenberger, A.; Obel, J.; Zhou, S.; Schlettwein, D.; Janek, J.; Meyer, B. K. LiPON Thin Films with High Nitrogen Content for Application in Lithium Batteries and Electrochromic Devices Prepared by RF Magnetron Sputtering. *Solid State Ionics* **2015**, *282*, 63–69.

(45) Pichonat, T.; Lethien, C.; Tiercelin, N.; Godey, S.; Pichonat, E.; Roussel, P.; Colmont, M.; Rolland, P. A. Further Studies on the Lithium Phosphorus Oxynitride Solid Electrolyte. *Mater. Chem. Phys.* **2010**, *123*, 231–235.

(46) Solano, M. A. C.; Dussauze, M.; Vinatier, P.; Croguennec, L.; Kamitsos, E. I.; Hausbrand, R.; Jaegermann, W. Phosphate Structure and Lithium Environments in Lithium Phosphorus Oxynitride Amorphous Thin Films. *Ionics (Kiel)* **2016**, *22*, 471–481.

(47) Brow, R. K.; Reidmeyer, M. R.; Day, D. E. Oxygen Bonding in Nitrated Sodium- and Lithium-Metaphosphate Glasses. *J. Non-Cryst. Solids* **1988**, *99*, 178–189.

(48) Wang, B.; Kwak, B. S.; Sales, B. C.; Bates, J. B. Ionic Conductivities and Structure of Lithium Phosphorus Oxynitride Glasses. *J. Non-Cryst. Solids* **1995**, *183*, 297–306.

(49) Marchand, R.; Agliz, D.; Boukbir, L.; Quemerais, A. Characterization of Nitrogen Containing Phosphate Glasses by X-Ray Photoelectron Spectroscopy. *J. Non-Cryst. Solids* **1988**, *103*, 35–44.

(50) Barsoukov, E.; Macdonald, J. R. *Impedance Spectroscopy: Theory, Experiment, and Applications*; 2<sup>nd</sup> ed.; John Wiley & Sons, Inc., 2005, 1–595, DOI: 10.1002/0471716243.

(51) Li, D.; Ma, Z.; Xu, J.; Li, Y.; Xie, K. High Temperature Property of All-Solid-State Thin Film Lithium Battery Using LiPON Electrolyte. *Mater. Lett.* **2014**, *134*, 237–239.

(52) Jacke, S.; Song, J.; Dimesso, L.; Brötz, J.; Becker, D.; Jaegermann, W. Temperature Dependent Phosphorous Oxynitride

Growth for All-Solid-State Batteries. *J. Power Sources* **2011**, *196*, 6911–6914.

(53) le Van-Jodin, L.; Ducroquet, F.; Sabary, F.; Chevalier, I. Dielectric Properties, Conductivity and  $\text{Li}^+$  Ion Motion in LiPON Thin Films. *Solid State Ionics* **2013**, *253*, 151–156.

(54) Mascaraque, N.; Fierro, J. L. G.; Durán, A.; Muñoz, F. An Interpretation for the Increase of Ionic Conductivity by Nitrogen Incorporation in LiPON Oxynitride Glasses. *Solid State Ionics* **2013**, *233*, 73–79.

(55) Jehnichen, P.; Wedlich, K.; Korte, C. Degradation of High-Voltage Cathodes for Advanced Lithium-Ion Batteries—Differential Capacity Study on Differently Balanced Cells. *Sci. Technol. Adv. Mater.* **2019**, *20*, 1–9.

(56) Shimizu, R.; Cheng, D.; Weaver, J. L.; Zhang, M.; Lu, B.; Wynn, T. A.; Burger, R.; Kim, M.-C.; Zhu, G.; Meng, Y. S. Unraveling the Stable Cathode Electrolyte Interface in All Solid-State Thin-Film Battery Operating at 5 V. *Adv. Energy Mater.* **2022**, *12*, 2201119.

(57) Rikarte, J.; Madinabeitia, I.; Baraldi, G.; Fernández-Carretero, F. J.; Bellido-González, V.; García-Luis, A.; Muñoz-Márquez, M. Á. AC Magnetron Sputtering: An Industrial Approach for High-Voltage and High-Performance Thin-Film Cathodes for Li-Ion Batteries. *Adv. Mater. Interfaces* **2021**, *8*, 2002125.

## Recommended by ACS

### Opportunities of Flexible and Portable Electrochemical Devices for Energy Storage: Expanding the Spotlight onto Semi-solid/Solid Electrolytes

Xiayue Fan, Jiujuan Zhang, *et al.*

OCTOBER 14, 2022  
CHEMICAL REVIEWS

READ 

### Toward a Mechanically Rechargeable Solid Fuel Flow Battery Based on Earth-Abundant Materials

Alexis M. Fenton Jr., Fikile R. Brushett, *et al.*

OCTOBER 25, 2022  
ACS OMEGA

READ 

### Thick Electrode Design for Facile Electron and Ion Transport: Architectures, Advanced Characterization, and Modeling

David J. Arnot, Esther S. Takeuchi, *et al.*

MARCH 22, 2022  
ACCOUNTS OF MATERIALS RESEARCH

READ 

### A Direct View on Li-Ion Transport and Li-Metal Plating in Inorganic and Hybrid Solid-State Electrolytes

Ming Liu, Marnix Wagemaker, *et al.*

JANUARY 13, 2022  
ACCOUNTS OF CHEMICAL RESEARCH

READ 

Get More Suggestions >